ASME Journal of Manufacturing Science and Engineering
Online journal at:
https://asmedigitalcollection.asme.org/manufacturingscience

Semih Akin
School of Mechanical Engineering,
Purdue University,
West Lafayette, IN 47907
e-mail: sakin@purdue.edu

Puyuan Wu
School of Mechanical Engineering,
Purdue University,
West Lafayette, IN 47907
e-mail: wu912@purdue.edu

Chandra Nath
School of Mechanical Engineering,
Purdue University,
West Lafayette, IN 47907;
Maijker Corp.,
West Lafayette, IN 47907
e-mail: chandra.nath@maijker.com

Jun Chen
School of Mechanical Engineering,
Purdue University,
West Lafayette, IN 47907
e-mail: junchen@purdue.edu

Martin Byung-Guk Jun[1]
School of Mechanical Engineering; Indiana Manufacturing Competitiveness Center (In-Mac),
Purdue University,
West Lafayette, IN 47907;
Maijker Corp.,
West Lafayette, IN 47907
e-mail: mbgjun@purdue.edu

A Study on Converging-Diverging Nozzle Design for Supersonic Spraying of Liquid Droplets Toward Nanocoating Applications

Supersonic cold spray (CS) of functional nanomaterials from atomized droplets has attracted significant attention in advanced thin-film coating as it enables particle deposition with high-adhesion strength. In CS, optimum design of the supersonic nozzle (i.e., converging-diverging nozzle) is essential for accelerating particles to desired velocities. However, research on the nozzle design for supersonically spraying of "liquid droplets" for nanocoating applications is limited. To this end, we investigate the effect of nozzle geometrical parameters, including throat diameter, exit diameter, and divergent length on droplets impact velocity by numerical modeling and experimental validation, followed by a case study on nanocoating. The discrete-phase modeling was employed to study droplets' flow behavior in continuous gas flow for various nozzle geometries. The results reveal that the nozzle expansion ratio, defined as a function of throat and exit diameters, has a significant influence on droplet velocity, followed by divergent length. Noteworthy, to correctly accelerate "low-inertia liquid microdroplets," it was found that the optimum nozzle expansion ratio for axisymmetric convergent-divergent nozzles should be in a range of 1.5–2.5, which is different and way smaller than the recommended expansion ratio (i.e., 5–9) for CS of conventional micron-scale "metal" powders. Based on the simulation results, an optimum design of supersonic nozzle is established and prototyped for the experimental studies. Particle image velocimetry (PIV) was used to experimentally investigate the spray flow field and to validate the numerical modeling results. Moreover, coating experiments using the optimized nozzle confirmed the effective supersonic spraying of droplets containing nanoparticles, thereby showing the potential for advanced nanocoating applications. [DOI: 10.1115/1.4062351]

Keywords: supersonic spraying, cold spray, droplet, numerical modeling, CFD, nanocoating, particle image velocimetry (PIV), additive manufacturing, advanced materials and processing, nontraditional manufacturing processes

1 Introduction

Supersonic cold spray (CS) coating is an emerging technique for the deposition of micro- and nanoparticles in a rapid and high-throughput manner. The scalability and the cost-effectiveness of this technique make it favorable for many applications such as transparent conductive films, solar cells, energy-storage materials, etc. [1]. In CS, the particles are accelerated to supersonic velocities through a converging-diverging nozzle (i.e., also known as de Laval nozzle) using compressed gases, then the particles impact a target surface, producing strong interfacial adhesion owing to the kinetic energy dissipation of the high-velocity impinging particles onto the target surface [1]. Herein, the supersonic nozzle is the backbone of the CS process to accelerate the coating materials to desired velocities prior to impact by generating a supersonic jet. The design of a supersonic nozzle also determines the deposition efficacy of the coating process.

The typical coating materials of CS are mainly gas-atomized "solid-state metal" microparticles (viz., copper, tin, zinc, etc.) [2]. Over the last decades, many endeavors have been made to optimally design of supersonic nozzles for spraying "metal particles" at desired velocities to achieve effective deposition on target surfaces [3–9]. Li et al. [4] studied the effect of nozzle geometry on particle acceleration in the CS process. Yin et al. [6] investigated the effect of different nozzle cross section shapes on gas flow and particle acceleration in CS. Sova et al. [10,11] scaled down the conventional CS nozzles by developing a micronozzle for high-resolution (i.e., 1 mm linewidth) deposition of aluminum particles. In these studies, the main focus was given on the CS of "solid-state metal" particles in a size range of 5–50 μm, and notable results regarding the nozzle design were reported to guide the researchers. Despite significant outputs, the conventional CS method is only applicable to micron-scale "metal" particles, and it is not applied to the supersonic CS of nanomaterials. The reasons behind that

[1]Corresponding author.

Manuscript received October 22, 2022; final manuscript received April 7, 2023; published online May 9, 2023. Assoc. Editor: Yong Chen.

are as follows: (1) insufficient inertia and momentum of solid-state nanopowders to penetrate the bow-shock region, which inherently appears around the target surface under the high-speed impact of spray jet [12,13]; (2) most of the nanomaterials (e.g., nanowires, nanorods) are only available as the colloidal "liquid" suspension that cannot be applied to traditional CS setups [14].

Recently, An et al. [1] altered the downstream injection of the conventional CS setup to be able to spray liquid-based nanomaterials (i.e., suspension or colloid) from atomized droplets. Through this approach, by using the atomized droplets as the carrying agent of nanoparticles, promising results in nanotechnology have been achieved, and it has paved the way for state-of-the-art applications [15,16]. In these studies, however, the fixed nozzle geometry was employed without considering the influence of nozzle design on the deposition process. Most recently, our group comprehensively studied the dispersion and deposition characteristics of micron-scale atomized "liquid droplets" under supersonic flow conditions for nanocoating applications by considering a specific nozzle geometry [14]. In that study, the validation of the numerical modeling for the supersonic spraying of droplets under various spraying conditions was confirmed, which then led to generalized parameter windows for supersonically spraying of droplets to provide useful information for the researchers. Given the nozzle design is the backbone of the CS process, a critical gap remains to understand the effect of nozzle geometrical parameters on "liquid droplets" behavior under supersonic flow conditions. Although many studies in the literature investigated optimum nozzle design for CS of conventional "solid-state metal particles" [3,5–10,17], to the authors' best knowledge, no research has been reported on how the nozzle design (i.e., nozzle geometrical parameters) affects the supersonic spraying of "liquid droplets" for nanocoating applications. Considering functional nanocoatings synergistically advance the field of smart thin films, understanding the influence of nozzle geometry on droplets flow behavior is vital to improving the efficacy of functional nanocoatings from atomized droplets. These are integral to the practical deployment of supersonic CS technique in nanocoating and advanced thin-film technology.

To this end, the present study is devoted to studying the influence of nozzle design on the droplets' flow characteristics under supersonic spray conditions. In this regard, numerical modeling (i.e., discrete-phase flow modeling) is setup to study the effect of the nozzle geometrical parameters on droplets' impact velocity under various flow conditions. This study addresses the effect of nozzle exit diameter (d_{ex}), nozzle throat diameter (d_{th}), and nozzle divergent length (L_{div}) on spray jet formation and droplets acceleration considering different droplet sizes in a range of 5–30 μm. The nozzle expansion ratio (i.e., the ratio of the areas of nozzle exit to throat, d_{ex}^2/d_{th}^2) was estimated from the corresponding nozzle exit and throat diameters to determine an optimum expansion ratio for an effective CS process. Based on the numerical modeling results, the optimal design of the supersonic nozzle is determined and prototyped. An experimental validation study and a case study on coating experiments using the optimized nozzle are then presented. The key and novel research contribution of this work is to draw insight into the nozzle design for supersonic CS of low-inertia micron-scale "liquid droplets" for functional nanocoating applications utilizing the droplets as the transport medium.

2 Materials and Methods

Numerical simulations were conducted through computational fluid dynamics (CFD) simulations by using ANSYS-FLUENT V19.1 to investigate the flow characteristic of the continuous gas (air) and discrete droplet phases. Water droplets were considered for the discrete phase due to the comparable similarity of water (i.e., density, viscosity) with most of the nanomaterial colloidal suspensions [14]. An axisymmetric (circular-shaped) nozzle configuration was selected owing to its widespread use in CS against rectangular-shaped and bell-shaped nozzles [18,19]. The nozzle dimensions and boundary conditions of the flow domain are presented in Figs. 1(*a*) and 1(*b*), respectively. The flow domain was discretized with the structured elements by using inflation layers to capture the boundary layer effects. The mesh (grid) structures at the nozzle throat and exit sections are illustrated in Fig. 1(*c*). Several mesh resolutions were employed to ensure mesh-independent solutions. Figure 2 shows the density distribution of the driving gas (air) along the nozzle axis for various mesh resolutions, which also presents insightful information on the compression of the gas upon impact to the substrate. As shown in Fig. 2, the density distribution is very similar for different mesh numbers, confirming the mesh-independent solutions for the henceforth analyses. Moreover, the y^+ value (i.e., non-dimensional distance from the wall of the first mesh node) was calculated as 29

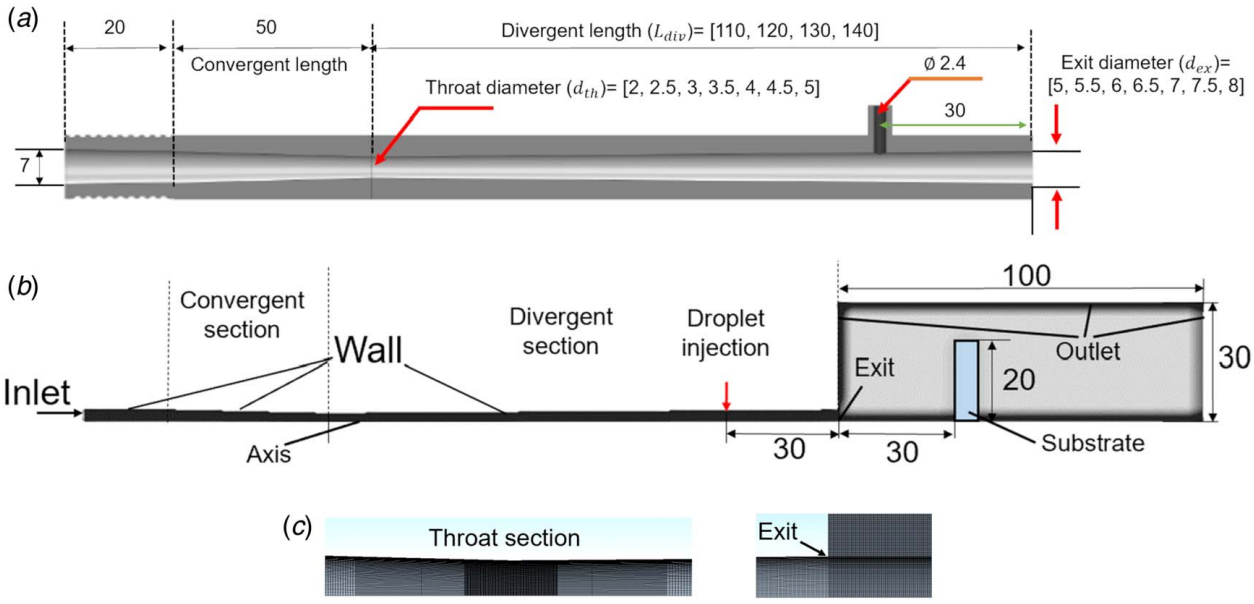

Fig. 1 Schematic of (*a*) the supersonic nozzle, (*b*) computational domain and boundaries, and (c) mesh (grid) structure at the nozzle throat (left panel) and the nozzle exit (right panel) (scale: mm)

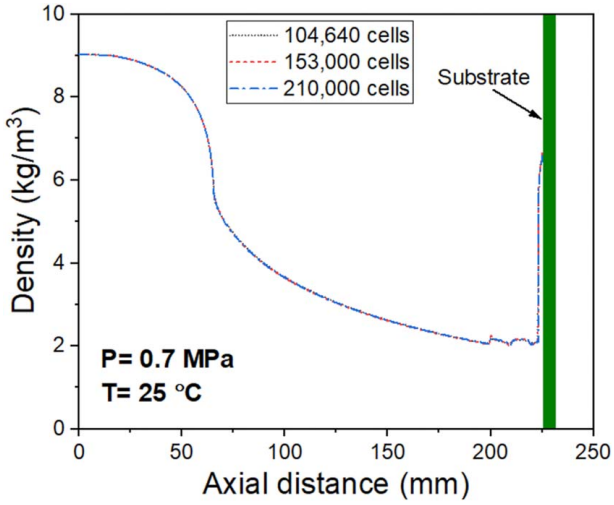

Fig. 2 Mesh independency test considering the density distribution of the driving gas (air) along the nozzle axis

Table 1 Boundary conditions

Location	Pressure (P)	Velocity (u)	Temperature (T)
Nozzle inlet	Specified	$\partial u/\partial n = 0$	Specified
Nozzle walls	$\partial P/\partial n = 0$	0	$\partial T/\partial n = 0$
Symmetrical axis	$\partial P/\partial r = 0$	$\partial u/\partial r = 0$	$\partial T/\partial r = 0$
Surrounding atmosphere	Ambient condition	$\partial u/\partial n = 0$	$\partial T/\partial n = 0$

for the discretized flow domain, indicating a suitable grid structure where the turbulent flow is dominant [20].

Following the discretization of the flow domain, a two-dimensional axisymmetric model was employed for the sake of low computational complexity and cost. A coupled discrete-phase modeling (i.e., Eulerian–Lagrangian approach) was used to track the droplets and investigate the droplets' acceleration for different nozzle geometrical configurations. The model was solved by using a steady-state pressure-based solver considering the compressibility effects of the continuous gas (air) phase. The realizable k–ε turbulence model with enhanced wall treatment was also incorporated into the model to consider the turbulence effects [20].

The boundary conditions of the model are given in Table 1. To elaborate, gas pressure and temperature were defined as the inlet boundary. The surface of the nozzle and the substrate were considered as adiabatic walls with no-slip boundary. In addition, the trap boundary condition was assigned to the nozzle walls and the substrate surface to capture the impinging droplets. The droplets were injected into the divergent section of the nozzle (i.e., 30 mm away from the nozzle exit) at ambient conditions without preheating. The outlet pressure was set to the atmospheric pressure (1 atm) at the nozzle exit and surroundings.

2.1 Continuous Phase (Driving Gas). The gas phase was modeled according to the Eulerian approach considering the compressibility effects of the driving gas flow. The governing equations of the continuous gas phase for a steady compressible turbulent flow (neglecting the gravitational forces) can be given as follows [13]:

Continuity equation:

$$\nabla \cdot (\rho \mathbf{u}) = S_m \tag{1}$$

Momentum equation:

$$\nabla \cdot (\rho \mathbf{u}\mathbf{u}) = -\nabla p + \nabla \cdot \bar{\bar{\tau}} + S_f \tag{2}$$

Energy equation:

$$\nabla \cdot (\rho e \mathbf{u}) = -p\nabla \cdot \mathbf{u} + \nabla \cdot (k\nabla \mathrm{T}) + \Phi + S_H \tag{3}$$

Species transport equations:

$$\nabla \cdot (\rho \mathbf{u} Y) = -\nabla \cdot \mathbf{J} + S_Y \tag{4}$$

$$\mathbf{J} = -\left(\rho D_m + \frac{\mu_t}{\mathrm{Sc}}\right)\nabla Y \tag{5}$$

Equation of state:

$$P = \rho RT \tag{6}$$

where ρ is the gas density (kg/m^3), $\mathbf{u}$ is the velocity (m/s), $\bar{\bar{\tau}}$ is the viscous stress tensor, p is the static pressure (Pa), e is the specific internal energy (J/kg), k is the thermal conductivity (W/(m · K)), T is the temperature, Y is the local mass fraction of the species, $\mathbf{J}$ is the mass diffusion flux (kg/(m^2 · s)) in turbulent flow, and μ_t is the turbulent viscosity (kg/(m · s)). S_m, S_f, S_H, S_y are the source terms to include the droplet evaporating species (i.e., water vapor in the air), droplet forces, and evaporation energy from the discrete phase, D_m is the diffusion coefficient for species in the mixture, and Sc is the Schmidt number.

2.2 Discrete Phase (Droplets). It is noteworthy that most of the nanomaterial solutions have similar physical properties with water at room temperature (e.g., silver nanoparticles dispersion ($\rho = 997$ kg/m^3 [21]), iron oxide nanoparticles ($\rho = 1000$ kg/m^3) [22], etc.). Also, the weight ratio of many nanomaterial solutions is ≤5%. For instance, silver nanoparticle dispersion in an aqueous buffer solution has a weight ratio of 2% [21] while iron oxide nanoparticle suspension has 5% [22]. The weight ratio of the stock nanomaterial solutions will be similar to the atomized droplets of these solutions. As such, in the present study, colloidal particles inside the droplets are neglected in the simulations under the aforementioned conditions. Thereby, the present study employs discrete-phase flow modeling (i.e., gas + droplets) to study the water droplets' behavior under supersonic flow conditions, and the continuum phenomenon is still valid. Notably, the droplet-droplet collision, breakup, and possible chemical reactions between the phases are beyond the scope of this work.

The Lagrangian approach was used to track the droplets inside the continuous phase flow by considering the interaction between the phases. The droplets velocity and trajectories were calculated by using Newton's second law as given in Eq. (7), where $\mathbf{u}_d$ is the droplet velocity (m/s), ρ_d is the droplet density (kg/m^3), and $\sum \mathbf{F}$ is the sum of hydrodynamic forces ; $\mathbf{F}_\mathrm{D}$ is the Stokes drag force, $\mathbf{F}_\mathrm{Ba}$ is the Basset force, $\mathbf{F}_\mathrm{VM}$ is the virtual mass force, $\mathbf{F}_\mathrm{Pg}$ is the pressure gradient force, $\mathbf{F}_\mathrm{Bu}$ is the buoyancy force, $\mathbf{F}_\mathrm{Saff}$ is the Saffman lift force, and $\mathbf{F}_\mathrm{Mag}$ is the Magnus lift force in the unit of Newton (kg · m/s^2). In this study, the drag force, Brownian force, and Saffman lift force were considered for micron-scale droplets. The Cunningham slip correction factor (C_c) given in Eq. (8) was also used to correct the Stoke's drag flow for micro-scale particles where d_p is the particle diameter (m), ρ_p is the particle density (kg/m^3), and λ is the molecular mean free path (m) [12].

To consider the heat transfer between the driving gas and the droplets, the conservation of energy equation given in Eq. (9) was considered where A is the surface area of the droplet (m^2), h_{fg} is the latent heat (J/kg), and h_c is the heat transfer coefficient (W/(m^{2}K)). The radiative heat transfer was neglected since the driving-gas temperature is relatively low in the divergent section of the nozzle due to the rapid expansion of the gas flow. The evaporation rate of the droplet was calculated using Eq. (10), where k_c is the mass transfer coefficient ((mol/s)/(m^2 · mol/m^3)), C_s is the vapor concentration at the droplet surface (g/m^3), and C_∞ is the vapor concentration of the flow (g/m^3). The heat transfer coefficient (h_c) and the mass transfer coefficient (k_c) were estimated by the empirical formulas given in Eqs. (11) and (12), respectively, where Nu is

the Nusselt number, Re is the Reynolds number, Pr is the Prandtl number, Sh is the Sherwood number, and Sc is the Schmidt number [23,24]. In addition, the discrete random walk (DRW) model [20] was employed to investigate the turbulent dispersion of the droplets in the spray flow and droplets trajectory by considering the instantaneous fluctuation of driving-gas velocity.

$$m_d \frac{d\mathbf{u}_d}{dt} = \sum \mathbf{F} = \mathbf{F}_{\mathrm{D}} + \mathbf{F}_{\mathrm{Ba}} + \mathbf{F}_{\mathrm{VM}} + \mathbf{F}_{\mathrm{Pg}} + \mathbf{F}_{\mathrm{Bu}} + \mathbf{F}_{\mathrm{Saff}} + \mathbf{F}_{\mathrm{Mag}} \tag{7}$$

$$C_c = 1 + \frac{2\lambda}{d_p}\left[1.257 + 0.4\exp\left(-\frac{1.1d_p}{2\lambda}\right)\right] \tag{8}$$

$$m_p c_p \frac{dT_p}{dt} = h_c A(T - T_p) + h_{fg}\frac{dm_p}{dt} \tag{9}$$

$$\frac{dm_p}{dt} = -Ak_c(C_s - C_\infty) \tag{10}$$

$$\mathrm{Nu} = 2 + 0.6\ \mathrm{Re}^{0.5}\mathrm{Pr}^{0.33} \tag{11}$$

$$\mathrm{Sh} = 2 + 0.6\ \mathrm{Re}^{0.5}\mathrm{Sc}^{0.33} \tag{12}$$

3 Simulation Results and Discussions

In CS, there exists a critical velocity for the particles' deposition on the target surface [25,26]. The particles exceeding the critical velocity undergo plastic deformation (bonding) upon impact on the target surface, resulting in a dense and strong adhesion coating [27,28]. In CS process, particle impact velocity is the main factor that decides the fate of the deposition. Hence, converging-diverging nozzles should be carefully designed to accelerate the particles above the critical impact velocity in CS applications. That said, in the current study, we study the influence of nozzle geometrical parameters on the droplets impact velocity by considering a comprehensive set of geometrical parameters and operational settings as listed in Table 2.

An optimal design of a supersonic nozzle should be performed for a fixed inlet gas pressure, and then the geometrical parameters (e.g., nozzle expansion ratio, divergent length) should be determined for that specific pressure value to achieve the maximum particle impact velocity [29]. Given that information, in this work, the influence of nozzle geometrical parameters on droplets impact velocity was studied at a driving-gas pressure of 0.7 MPa to be consistent with our previous study [14]. The nozzle expansion ratio was also tested for a different inlet gas pressure (i.e., 0.5 MPa) at various driving-gas temperatures. The parameters involved in CFD simulations are listed in Table 2. The ranges of the parameters in Table 2 were selected considering the suggestions on converging-diverging nozzle design [4,5,17,30] and operational settings for the supersonically spraying of droplets containing functional nanomaterials [31]. Moreover, considering thin-film coatings are widely applied to the low-thermal budget polymer substrates (e.g., PET, PEN) for printed electronics and smart sensing applications [32,33], we intentionally chose a relatively low inlet temperature range of the driving gas from 25 °C to 200 °C. Furthermore, it is noteworthy to state that the dimensions of the stagnation chamber and convergent section of the nozzle were considered constant as 20 mm and 50 mm, respecively since the convergent section has a negligible effect on particle impact velocity [4].

Table 2 Parameters involved in the simulations

Throat diameter, d_{th}, (mm)	2, 2.5, 3, 3.5, 4, 4.5, 5
Exit diameter, d_{ex}, (mm)	5, 5.5, 6, 6.5, 7, 7.5, 8
Divergent length, L_{div}, (mm)	110, 120, 130, 140
Droplet diameter (μm)	5, 10, 15, 20, 25, 30
Driving gas pressure (MPa)	0.5, 0.7
Driving gas temperature (°C)	25, 100, 200

3.1 Effect of Nozzle Throat Diameter on Droplet Velocity.

Figures 3(*a*) and 3(*b*) show the effect of the nozzle throat diameter on the average upon-impact velocity of droplets considering two different nozzle exit diameters (i.e., $d_{ex} = 6.5$ and 5.5 mm) for various droplet sizes. The gas inlet pressure and nozzle divergent length are set to be constant at 0.7 MPa and 130 mm, respectively. One important finding is that there exists a maximum droplet velocity for a certain nozzle configuration for any droplet sizes that are considered. The highest droplet velocity of 471 m/s was obtained for the throat diameter of 4.5 mm and exit diameter of 6.5 mm (Fig. 3(*a*)) as compared to the highest velocity of 465 m/s for the combination of 3.8 mm throat and 5.5 mm exit diameters (Fig. 3(*b*)).

Another important finding in Figs. 3(*a*) and 3(*b*) is that droplets experience a much lower impact velocity for the throat diameters of 2, 2.5, and 3 mm as compared to larger throat diameters. It is attributed to the formation of normal shock waves inside and outside of the nozzle (see Fig. 5(*a*)). To elaborate, the nozzles with smaller throat diameters (i.e., 2, 2.5, and 3 mm) generate over-expanded spray jet, resulting in lower droplets' impact velocities due to the severe fluctuation in the gas pressure (Fig. 5(*c*)). The shock waves start to develop within the nozzle for the over-expanded jet, and eventually decelerate the gas flow velocity at the nozzle exit (see Fig. 5(*a*) for $d_{th} = 2$, 2.5, and 3 mm). This phenomenon can be better observed in Figs. 5(*c*) and 5(*d*), in which the gas pressure oscillates at the nozzle exit for the $d_{th} \leq 3.5$ mm. Conversely, for the under-expanded jet flow (Fig. 5(*a*) for $d_{th} = 3.5$, 4, and 5 mm), the gas velocity is higher than the over-expanded nozzle configuration at the nozzle exit, which explains the higher droplets' impact velocity for these nozzle geometries (see Figs. 3(*a*) and 3(*b*)). Pressure distribution of the gas flow along the nozzle central axis in Figs. 5(*c*) and 5(*d*) also correlates with these results as comparatively less fluctuation in gas pressure for the over-expanded jet observed when $d_{th} > 3.5$ mm. Moreover, droplets at $\leq 10\ \mu$m are more susceptible to normal shock waves under over-expanded spray flow (see Figs. 3(*a*) and 3(*b*)) for $d_{th} = 2$, 2.5, and 3) as compared to the under-expanded nozzle configuration. These results suggest that a nozzle having over-expanded jet flow is not a suitable choice for supersonically spraying of low-inertia particles like liquid droplets.

The highest droplet velocity was obtained at a throat diameter of 4.5 mm for the correctly-expanded nozzle configuration (enclosed image in Fig. 5(*a*)), which also has the minimum shock wave formation along the nozzle with minimal pressure oscillation at the nozzle exit (see $d_{th} = 4.5$ mm in Fig. 5(*c*) and $d_{th} = 5$ mm in Fig. 5(*d*)). It implies that shock waves have a critical impact on the acceleration of micron-scale low-inertia liquid droplets in the supersonic spraying process, which can be controlled by the throat diameter. The results are consistent with the literature concluding that undesirable shear layers, expansion fans, and shock waves intrinsically form if the nozzle is not designed in a correctly-expanded manner [9].

3.2 Effect of Nozzle Exit Diameter on Droplet Velocity.

Figures 3(*c*) and 3(*d*) show the effect of nozzle exit diameter on droplets' average impact velocity for different throat diameters. It was observed that the nozzle exit diameter is as not critical as the throat diameter for droplet acceleration since the rapid expansion of the gas starts from the throat section and develops through the divergent part. The maximum droplet velocity was obtained for the nozzle having $d_{ex} = 6.5$ mm when $d_{th} = 4.5$ mm (Fig. 3(*c*)), and $d_{ex} = 5$ mm when $d_{th} = 3.5$ mm (Fig. 3(*d*)).

Another important finding from Figs. 3(*a*)–3(*d*) is that droplets' size also significantly influences droplet velocity. A decrease in droplet diameter leads to higher impact velocities, particularly for the droplets having a diameter of $\leq 15\ \mu$m. On the one hand, the increase in droplet velocity for the larger droplets ($\geq 15\ \mu$m) is not

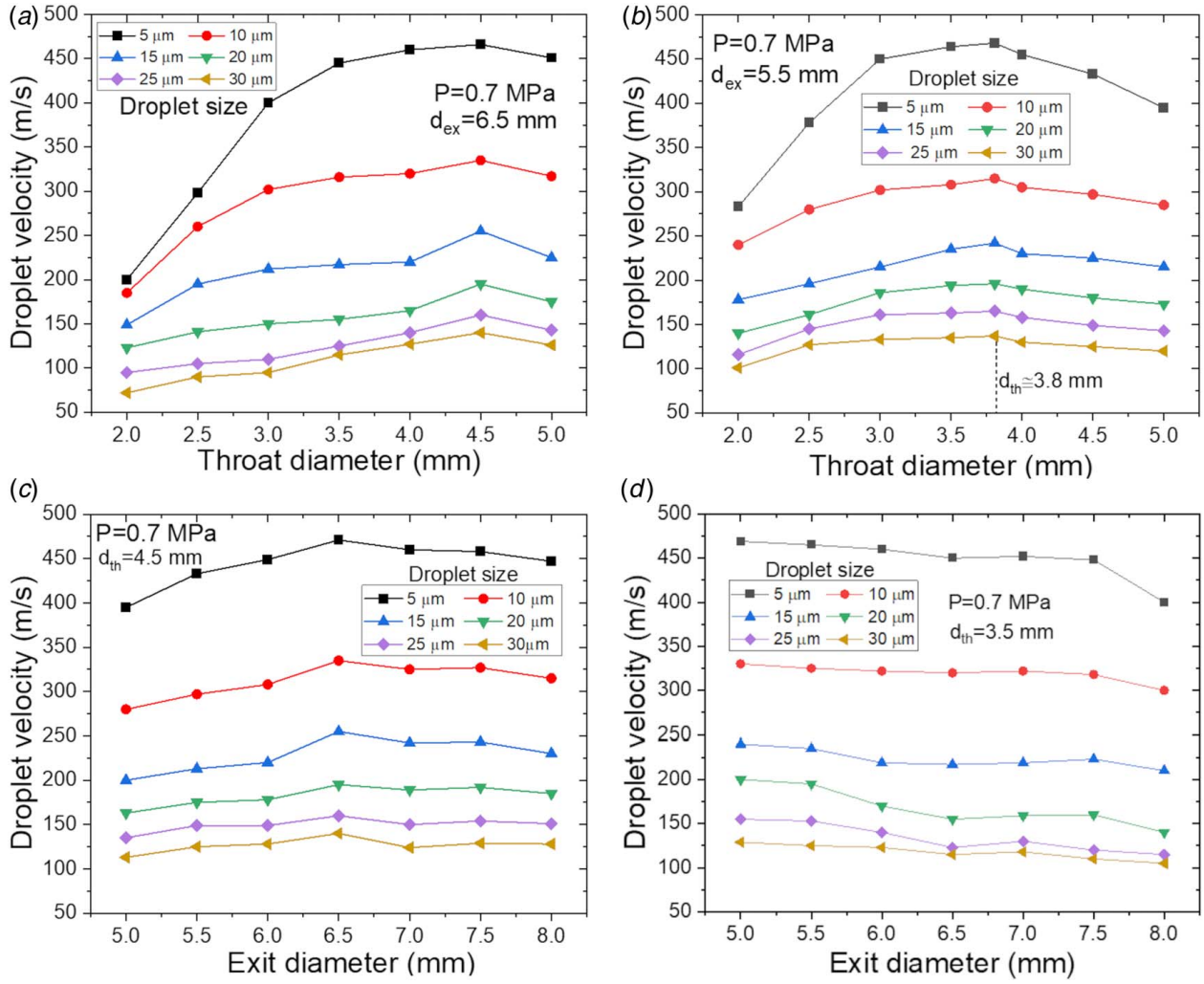

Fig. 3 Effect of the nozzle throat diameter and exit diameter on droplet impact velocity: (*a*) $P = 0.7$ MPa, $d_{ex} = 6.5$ mm, (*b*) $P = 0.7$ MPa, $d_{ex} = 5.5$ mm, (*c*) $P = 0.7$ MPa, $d_{th} = 4.5$ mm, and (*d*) $P = 0.7$ MPa, $d_{th} = 3.5$ mm ($T = 300$ K and $L_{div} = 130$ mm for all analyses)

as remarkable as smaller droplets, which is likely attributed to the high inertia of larger droplets. The traditional CS feedstock powders (i.e., solid-state metal particles) also follow a similar flow behavior, having a decreasing impact velocity for larger metal particles [34,35]. These results reveal that the smaller droplets could be preferred if there is a need for higher droplets impact velocity in the supersonic CS process.

3.3 Effect of Nozzle Expansion Ratio on Droplet Velocity. The nozzle expansion ratio (i.e., the ratio of the cross-sectional areas of nozzle exit to the throat, d_{ex}^2/d_{th}^2) was calculated to investigate the combined effect of nozzle throat and exit diameters on droplets' impact velocity. As shown in Figs. 4(*a*)–4(*f*), for any droplet size, there exists an optimum nozzle expansion ratio at certain inlet gas pressure to effectively accelerate the low-inertia droplets to supersonic velocities. The highest velocity of droplets was obtained for the nozzle expansion ratio of 2.086 and 2.04 at inlet gas pressures of 0.7 MPa and 0.5 MPa where $T = 25$ °C, respectively (see Figs. 4(*a*) and 4(*b*)). Both results correspond to the spray jet with minimum shock wave formation and turbulent velocity fluctuation inside and outside of the nozzle (see Figs. 5(*a*) and 5(*b*)).

We also studied the combined effect of gas temperature and nozzle expansion ratio on droplets velocity. As shown in Figs. 4(*a*)–4(*f*), higher driving-gas temperatures led to higher droplets impact velocity. It is attributed to the internal energy gain of the droplets at higher gas temperatures, which resulted in greater droplets impact velocity [17]. Although the droplets velocity increased with increasing gas temperature, the optimal nozzle expansion ratio did not change for different gas temperatures. The results indicate that the optimal nozzle expansion ratio is mainly affected by the inlet gas pressure, not the gas temperature.

Previous studies on traditional CS reported that the typical value of nozzle expansion ratio for supersonically spraying of micron-scale "solid-state particles" should be in a range of 5–9 to have the Mach number of 2–3.5 at the nozzle exit [11]. In the present study, however, we interestingly observed that the optimum nozzle expansion ratio for supersonically spraying of low-inertia micron-scale "liquid droplets" is in a range of 1.5–2.5, which is different than the suggested value of nozzle expansion ratio in Ref [11] for traditional CS feedstock material of "metal powders." This study reveals that micron-scale liquid droplets behave differently under supersonic flow as compared to typical feedstock materials (i.e., metal microparticles) of CS process. As a noteworthy result, microdroplets do not obey the recommendations on the optimal expansion ratio of the CS nozzle design suggested in the literature for CS of typical metal particles [11,25]. Besides, the droplets are more susceptible to turbulent velocity fluctuation and normal shock wave formation compared to metal particles due to droplets' lower inertia as compared to metal microparticles. As such, the geometrical parameters of a converging-diverging nozzle should be carefully selected for effective supersonic spraying of droplets containing functional nanomaterials. Taken all together, the ideal design of a converging-diverging nozzle to supersonically spray

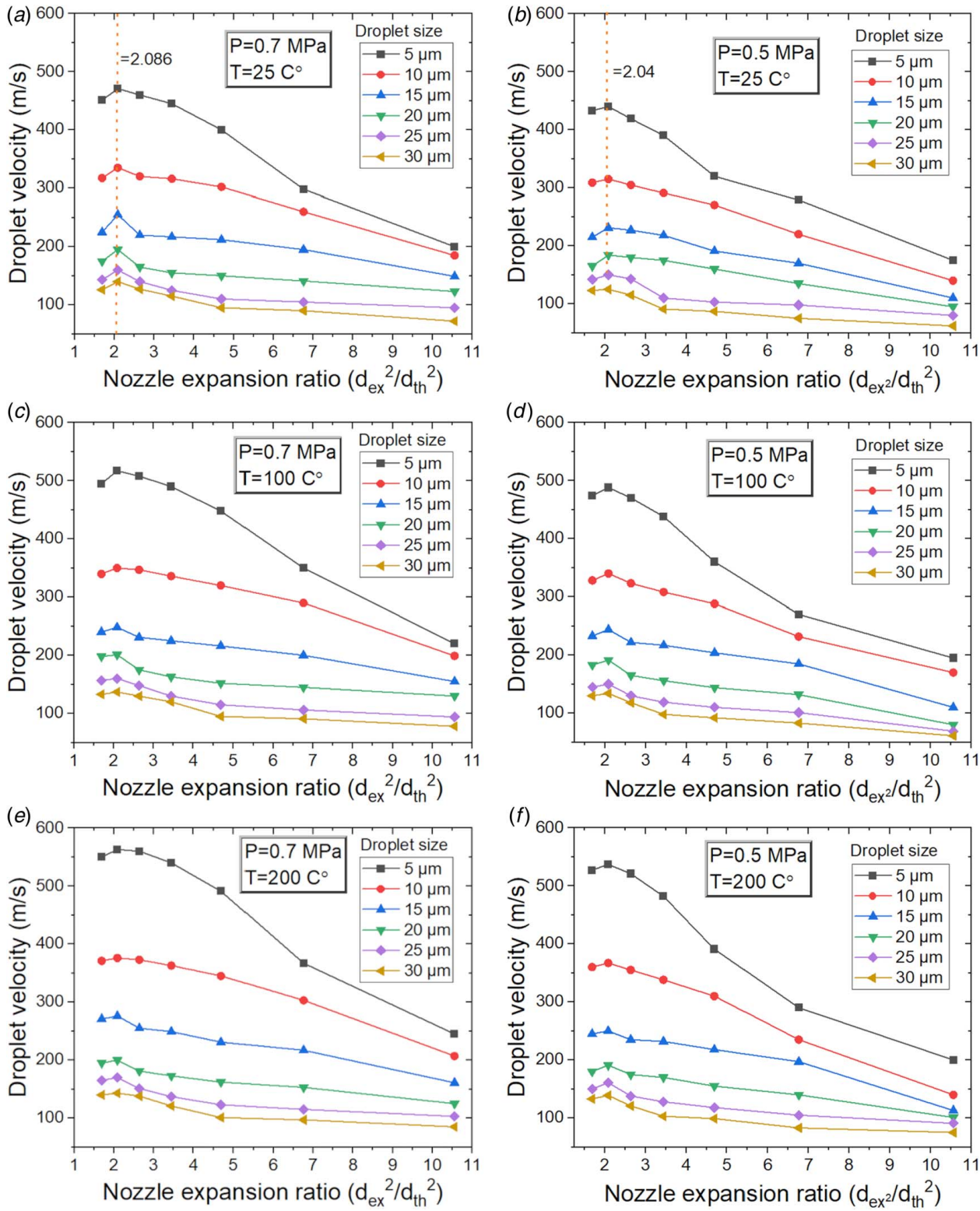

Fig. 4 Effect of the nozzle expansion ratio on droplet impact velocity at various gas inlet conditions: (*a*) $P = 0.7$ MPa, $T = 25$ °C, (*b*) $P = 0.5$ MPa, $T = 25$ °C, (*c*) $P = 0.7$ MPa, $T = 100$ °C, (*d*) $P = 0.5$ MPa, $T = 100$ °C, (*e*) $P = 0.7$ MPa, $T = 200$ °C, (*f*) $P = 0.5$ MPa, $T = 200$ °C, and ($L_{div} = 130$ mm for all analyses)

low-inertia droplets should possess correctly-expanded flow with minimum shock wave formation and turbulent velocity fluctuation, having an optimal expansion ratio at a specific driving-gas inlet pressure.

3.4 Effect of Nozzle Divergent Length on Droplet Velocity. The previous studies on supersonic nozzle design for CS of metal particles reported that nozzle divergent length has an important influence on micron-scale particle acceleration [4]. Especially, the divergent length should be long enough to provide an ideal accelerating path for the particles in the gas flow [11]. However, a very high value of divergent length leads to a drop in gas velocity due to the boundary layer growing on the nozzle walls [11]. Thus, the ratio between the divergent length and nozzle exit diameter

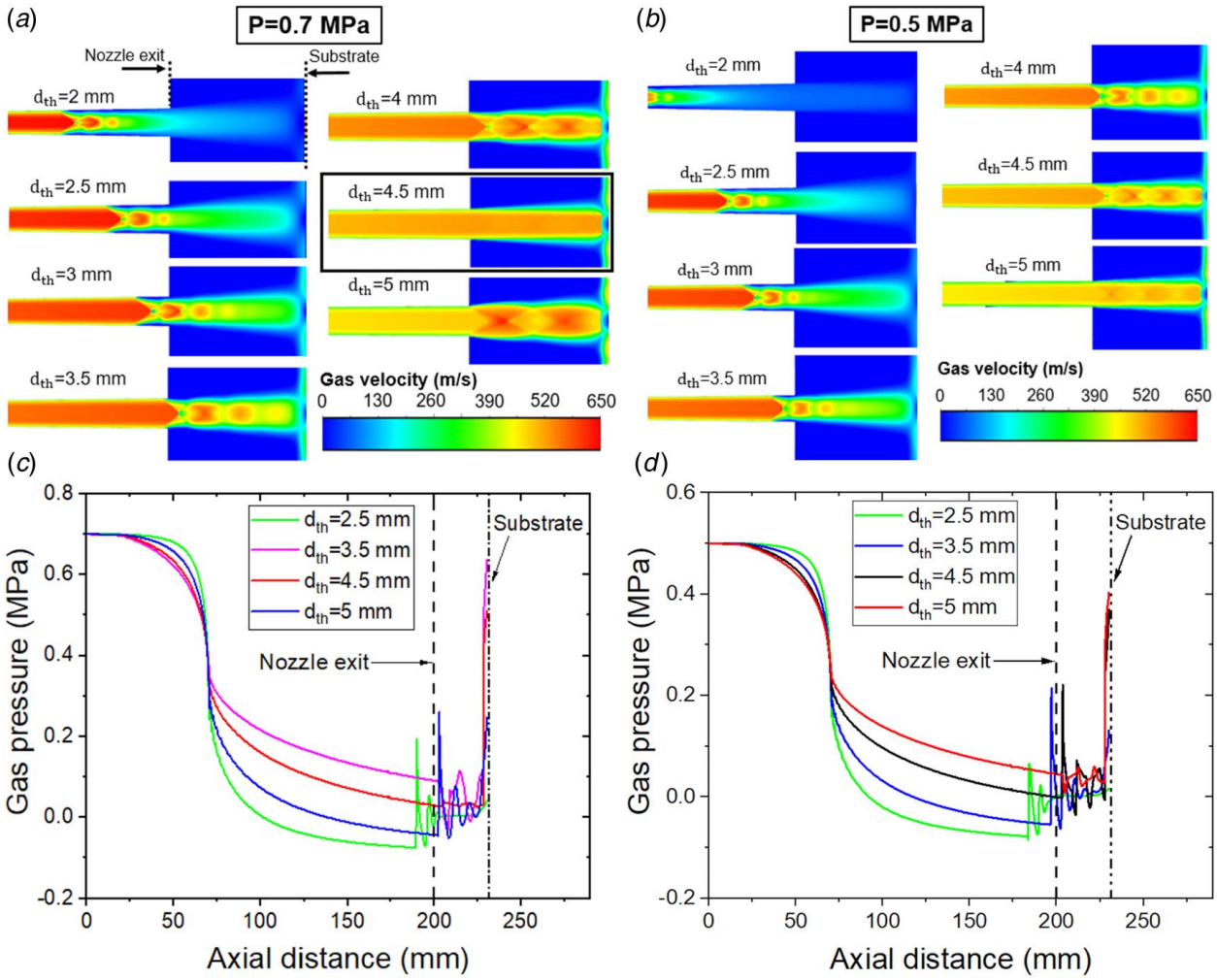

Fig. 5 Contours of the driving gas velocity with shock wave formations for different nozzle throat diameters at (*a*) $P = 0.7$ MPa and (*b*) $P = 0.5$ MPa. Pressure (gauge) distribution of the driving gas along the nozzle central axis at (c) $P = 0.7$ MPa and (*d*) $P = 0.5$ MPa conditions ($L_{div} = 130$ mm and $d_{ex} = 6.5$ mm for all analyses).

(L_{div}/d_{ex}) determines the convenient acceleration of the particles [11]. In particular, the literature suggests that the typical value of L_{div}/d_{ex} for a supersonic spray nozzle for suitable particle acceleration should be in a range of 15–20 [11,36].

In this study, based on the abovementioned information, various divergent lengths (i.e., 110, 120, 130, 140 mm) were selected to analyze the effect of divergent length on droplet acceleration by keeping the nozzle exit diameter, d_{ex}, constant as 6.5 mm. As shown in Fig. 6, shorter divergent lengths (i.e., $L_{div} = 110$ and 120 mm) resulted in lower droplet velocities. The reason lies in the shorter/insufficient acceleration path of the droplets in the supersonic section (diverging section) of the nozzle. The maximum droplets velocities were obtained for the nozzle having a divergent length of 130 mm. For this nozzle configuration, the ratio of L_{div}/d_{ex} is estimated to be 20, which is consistent with the studies on CS of micron-scale metal particles [11,36]. Further increase in divergent length (i.e., $L_{div} = 140$) led to a decrease in droplet velocity, which is attributed to the boundary layer growing (friction) phenomenon on the nozzle walls [11]. Thereby, it can be concluded that supersonically spraying of micron-scale droplets obeys the recommendations on the selection of divergent length for traditional CS feedstock of metal microparticles.

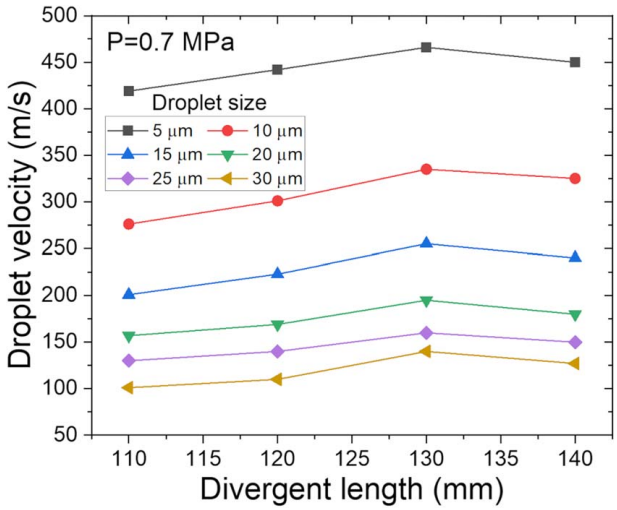

Fig. 6 Effect of the nozzle divergent length on droplet velocity ($d_{th} = 4.5$ mm and $d_{ex} = 6.5$ mm)

4 Experimental Correlation

4.1 Experimental Details. Based on the CFD simulations, the optimum design of the converging-diverging nozzle was determined for an inlet gas pressure of 0.7 MPa and then developed a prototype as shown in Fig. 7(*a*). An atomization-assisted supersonic spray system, as presented in Fig. 7(*b*), was also constructed for particle image velocimetry (PIV) measurements and coating

experiments to justify the numerical modeling results and test the nozzle performance. The spray setup consists of two separate modules: (i) the atomization unit and (ii) the supersonic nozzle (Fig. 7(*b*)). In spraying experiments, first, nanomaterial suspension is atomized into micron-scale droplets through a low-pressure gas flow in the atomization chamber. Next, the droplets are carried into the nozzle injection port by a low-pressure carrier gas flow. Lastly, the central high-pressure central gas flow accelerates the droplets to supersonic velocities and focuses them onto the target surface. Through this configuration, our approach distinctly differentiates from traditional AJP [37] in two ways: (1) it employs the supersonic jet stream; (2) it does not require dedicated vacuum equipment. Moreover, owing to the supersonic jet stream, the functional nanoparticles can be successfully deposited through deep and narrow channels (1 μm linewidth) with improved adhesion strength [38], which is crucial in such applications (e.g., laser-direct writing of polymers and glass). The operational settings of the spray experiments are presented in Table 3.

The PIV technique was used to capture the velocity profile of the sprayed droplets at the downstream of the nozzle exit. Figure 7(*c*) illustrates the PIV setup that consists of a dual Nd:YAG pulse laser (EverGreen EVG00200, wavelength 532 nm, pulse length of 6 ns, maximum energy of 200 mJ per pulse), a group of optical lenses (Thorlabs), and a charge-coupled device (CCD) camera (Imperx Bobcat 1620, 1600 × 1200 pixels) equipped with a Nikkor 60 mm lens. In PIV measurements, two laser pulses create a light sheet through the optical lenses to illuminate the center plane of the spray flow field with a time interval (dt) of 1 μs. The double-exposed images were processed by using commercial software (LAVISION DAVIS 8.4) with an auto-correlation algorithm given in Eq. (13), where I is the light intensity in a selected area of M pixels by N pixels in a PIV image (i.e., known as the correlation window), i and j denote the pixel's location in the correlation window. The location of the correlation map's peak value was calculated by Eq. (14), which corresponds to the displacement of the droplets in the selected window during the time interval. As such, the droplets' velocity (u) was then calculated by Eq. (15) in the direction of atan(dy/dx). Lastly, the velocity field was obtained by transversing the correlation window across the flow field and repeating the procedure [39]. In the present study, the initial size

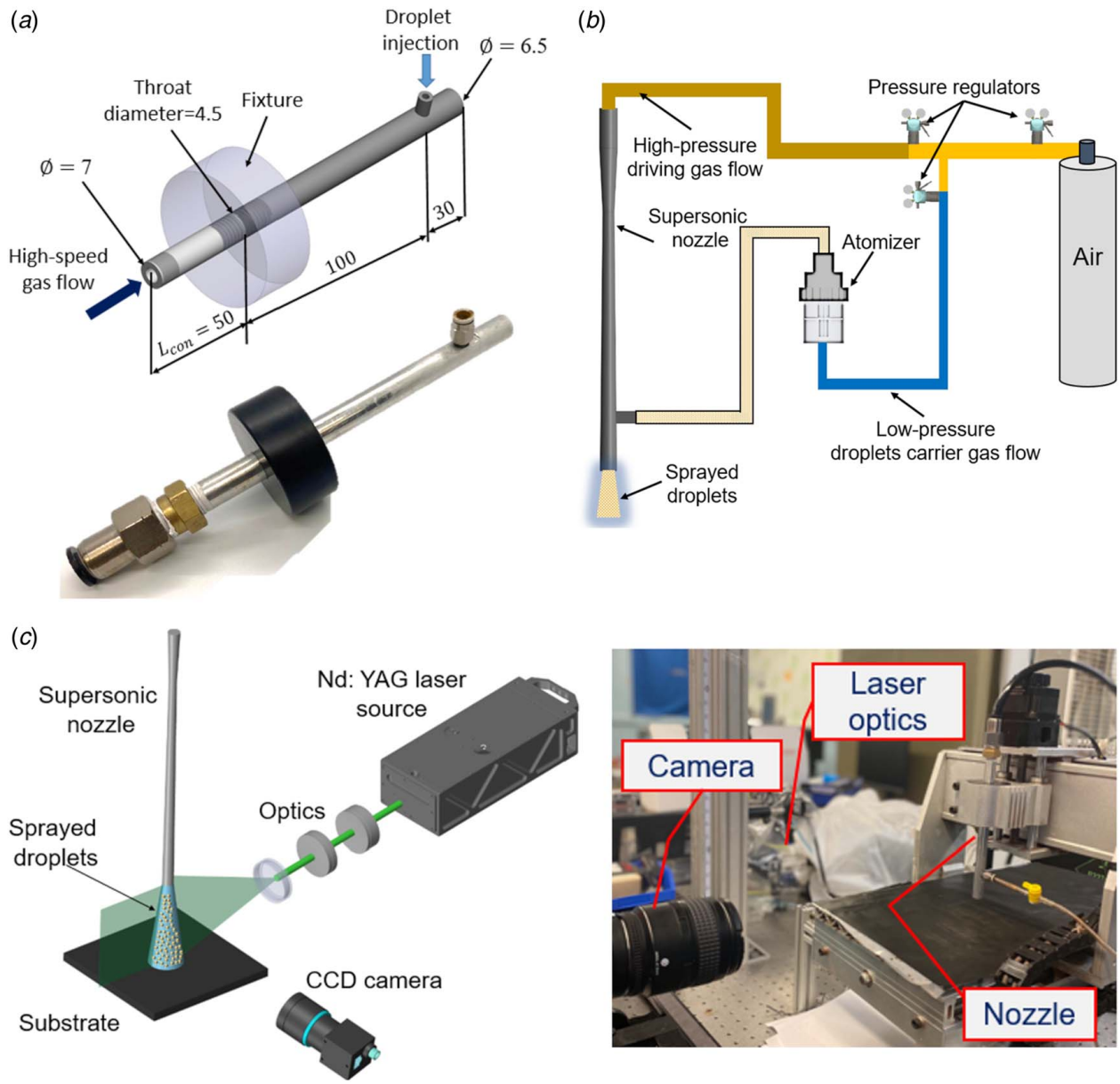

Fig. 7 (*a*) Optimized supersonic nozzle, (*b*) spray setup, and (*c*) PIV setup (scale: mm)

Table 3 Operational settings of the spray experiments

Parameter	Setting
Driving and carrier gas	Air
Gas inlet pressure (MPa)	0.7
Gas inlet temperature (°C)	25 (room temperature)
Atomization pressure (kPa)	70
Spray distance (mm)	10, 30, 50

of the correlation window is 128 by 128 pixels with 50% overlapping in both directions, and the algorithm iterates thrice. The correlations window then shrinks to 64 by 64 pixels and the algorithm iterates twice to capture the droplets velocities and the flow field. Overall, the CCD camera recorded a total of 2000 double-exposed images to calculate the droplets' velocity. The velocity vectors of droplets were then calculated and plotted for comparison with numerical modeling results. A clear PIV image of the sprayed droplet stream can be seen in Fig. 8(*a*).

$$\varepsilon(\Delta x, \Delta y) = \sum_{i=-M/2}^{M/2} \sum_{j=-N/2}^{N/2} I(i,j)I(i+\Delta x,\ j+\Delta y) \tag{13}$$

$$(dx, dy) = \text{argmax}(\varepsilon(\Delta x, \Delta y)) \tag{14}$$

$$u = \sqrt{dx^2 + dy^2}/dt \tag{15}$$

Following the PIV measurements, surface coating experiments were also performed to show the utility and applicability of the optimally designed nozzle for nanocoating applications. In this regard, a titanium dioxide (TiO_2) nanomaterial suspension (i.e., well-dispersed TiO_2 nanoparticles (NanoAmor Inc, Texas, USA) in deionized water) was prepared and used to visualize the resultant coatings. The prepared suspension was then atomized into fine micron-scale droplets and sprayed onto a polymer substrate (i.e., indium tin oxide coated polyethylene terephthalate (ITO/PET)), which is widely used in solar cell applications as the photoanode material. The width of the coatings was predicted from the CFD simulations by capturing the trajectories of the impinging droplets. The results were then compared with the actual width of single-pass coatings obtained from the coating experiments using the spray setup in Fig. 7(*b*).

4.2 Experimental Results and Discussions. In the numerical simulations under this section, a droplet stream having the Rosin–Rammler size distribution was injected into the divergent section of the nozzle, and trajectories of the droplets were then tracked. The Rosin–Rammler size distribution is given in Eq. (16) [20]

$$Y_d = e^{-(d/\bar{d})^n} \tag{16}$$

where d is the droplet diameter, $\bar{d}$ is the mean droplet diameter, n is the size distribution parameter, and Y_d is the mass fraction of droplets. The abovementioned size distribution parameters were selected from the atomizer's technical specifications. In detail, a commercial pneumatic jet nebulizer (VixOne, Westmed, USA) [40] was employed to atomize the water (for the PIV tests) and TiO_2 dispersion (for the nanocoating experiments) into the micron-scale fine droplets. This atomizer has a mass median aerodynamic diameter of 2.7 μm [40], which can also generate droplets with a maximum diameter of $\approx$10 μm [41,42]. Moreover, a stochastic tracking model, DRW [43], was employed to capture the velocity and trajectory fluctuations of the droplets under turbulent dispersion. The DRW model predicts the fluctuations of the droplets velocity and its effects on droplets trajectory [20]. Coupling the Rosin–Rammler size distribution with the DRW model enabled us to calculate the velocity and trajectory distribution of the droplets at the nozzle exit with standard deviations for a better comparison with the experimental measurements. Lastly, the CFD simulations were then compared with the PIV-measured velocity data followed by the surface coating experiments.

Figure 8(*a*) shows the PIV-measured droplet velocity vector field from the nozzle exit to the downstream of 28 mm (i.e., 2 mm right before the impingement). On the one hand, Fig. 8(*b*) shows the droplets' velocity trajectories at the nozzle exit obtained from the CFD simulations. Both CFD and PIV results show that the droplets are successfully accelerated to supersonic velocity using the optimally designed nozzle. Moreover, the CFD results of droplets velocity distribution are in agreement with the PIV data, showing comparable spray morphology.

Figure 8(*c*) compares the CFD results with the PIV-measured averaged velocity data along the radial direction of the nozzle exit for various downstream distances. Both simulation and experimental (PIV) results showed a similar and comparable trend in droplet velocity. The numerical CFD simulations, however, predicted the droplets' velocity relatively higher than the PIV results. This can be attributed to: (i) the absence of a more precise droplet injection port in the flow domain; and (ii) the two-dimensional axisymmetric flow assumption in modeling. Taken together, the numerical modeling results are comparable with the experimental PIV

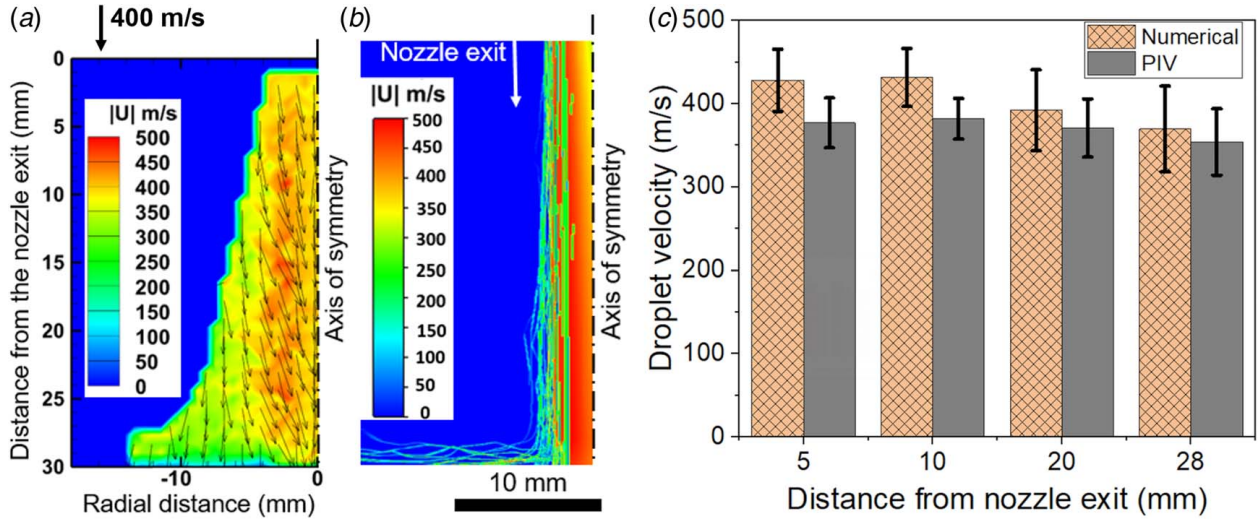

Fig. 8 (*a*) The PIV-measured velocity of distribution droplets, (*b*) velocity contour of droplets predicted by the numerical simulations, and (*c*) comparison of the PIV and numerical modeling results

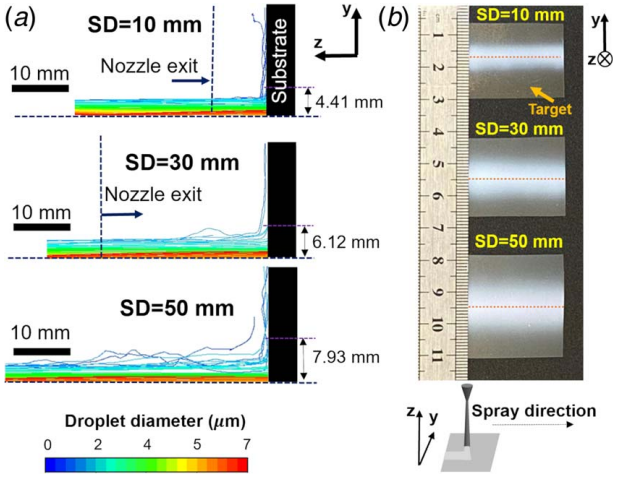

Fig. 9 (*a*) Droplet trajectories for different SD and (*b*) images of the resultant TiO_2 coatings

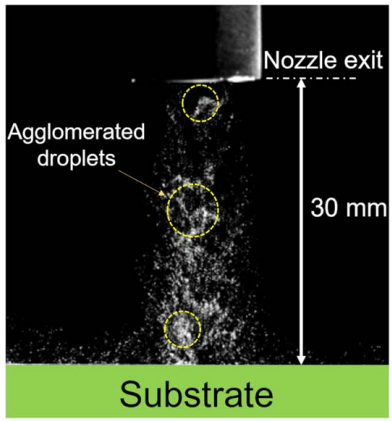

Fig. 10 A CCD camera image of the droplet stream at SD = 30 mm

measurements presenting similar trends for the velocity distribution of the droplets at the nozzle exit.

The coating experiments were also performed by employing commercial TiO_2 nanoparticles (see Fig. 11(*a*)) in a suspension to further test the numerical modeling and optimized nozzle for actual spray coating scenarios. The coating experiments were performed using a computer programmable stage to accurately spray the droplets containing nanoparticles. The nozzle transverse speed was set to 20 mm/min and a single spray pass was applied at different spray distances (SD) (i.e., nozzle stand-off distances) from 10 mm to 50 mm. The coating results were then compared with the CFD simulation for various spray distances.

Figure 9(*a*) shows the droplet trajectories for the half-portion of the nozzle for different droplet sizes acquired from numerical simulations. On the one hand, Fig. 9(*b*) illustrates the resultant experimental coatings on the substrate at different spray distances. The

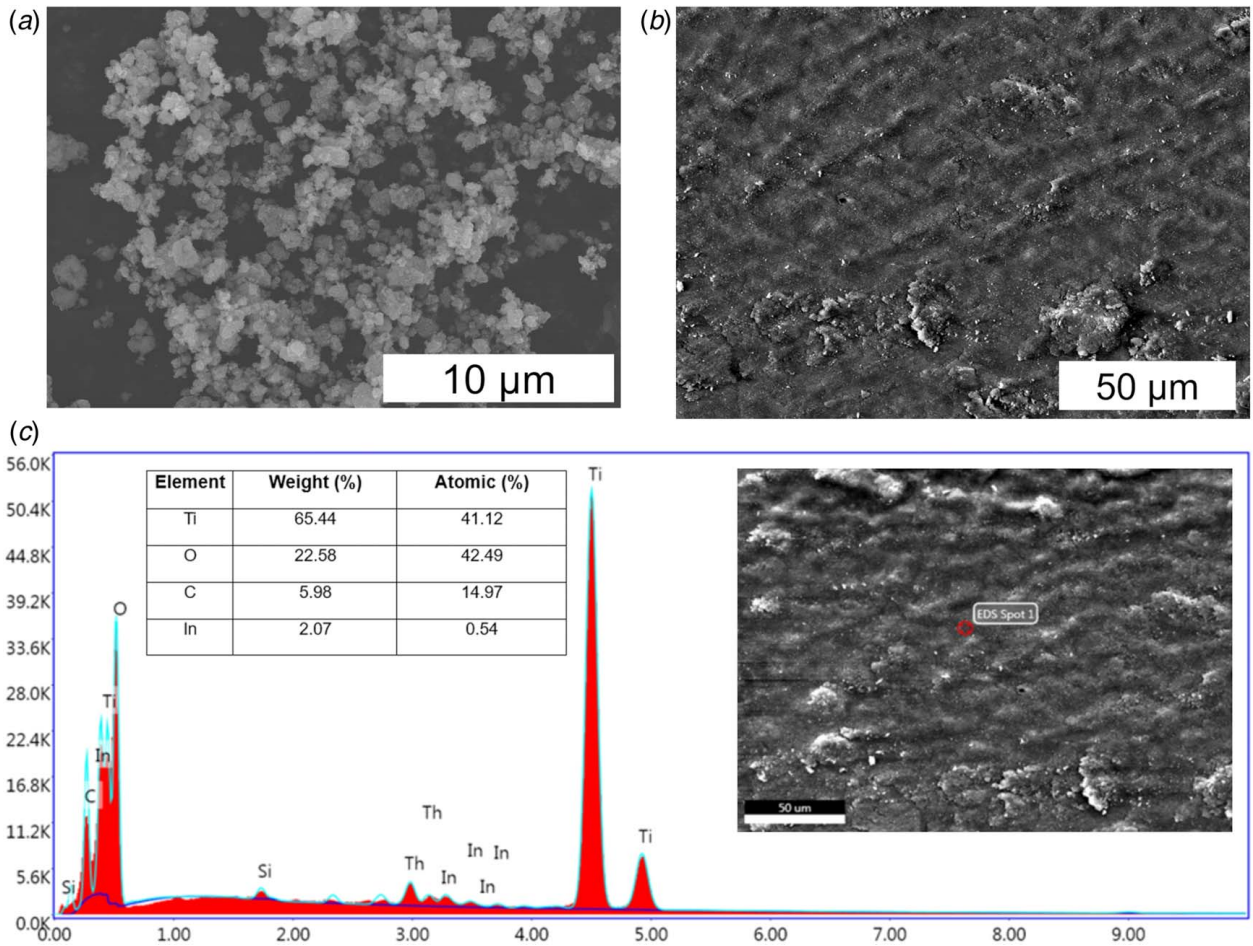

Fig. 11 Microstructure characterizations: (*a*) morphology of the TiO_2 nanoparticles, (*b*) surface microstructure of the resultant TiO_2 film on the ITO/PET surface after supersonic spraying, and (c) EDX analysis of the resultant TiO_2 nanocoating

main objective of Figs. 9(*a*) and 9(*b*) is to compare the numerical modeling results with coating experiments in terms of coating width. In this regard, the sprayed droplets are tracked via numerical modeling, and the coating width was then predicted from impingement trajectories of the droplets on the target surface for each SD.

As shown in Figs. 9(*a*) and 9(*b*), an increase in SD prompts the droplet dispersion onto the substrate, resulting in a lower spray resolution. The high dispersion characteristic of droplets onto the substrate surface for a longer SD is mainly responsible for this phenomenon. Another noteworthy finding is that larger droplets better focus near the axis of the nozzle (see Fig. 9(*a*)), leading to a thicker deposition at the central region of the coating as shown in Fig. 9(*b*). A possible reason for this could be the agglomeration of droplets in the nozzle after their injection. A CCD camera image in Fig. 10 reveals that the droplets locally agglomerate (i.e., merge in-flight) at the central region of the nozzle during spraying. It is likely attributed to the intensive mixing of the gas phase (air) and discrete phase (droplets) under the supersonic flow, which could propagate the collision of the droplets, thereby forming larger agglomerates [44,45]. As such, the droplets form larger sizes at the near central region of the nozzle due to agglomeration, leading to a denser particle deposition on the target surface along the central trajectory. The coating density, however, gradually decreases toward the outer region of the nozzle axis. It is attributed to the impingement of smaller droplets onto the outer side of the nozzle axis due to the susceptible nature of smaller droplets in the turbulent flow.

Scanning electron microscopy (SEM, Hitachi S-4800) and energy dispersive X-ray spectroscopy (EDX) analyses were also conducted to investigate the microstructure of the resultant coatings. As shown in Fig. 11(*b*), the as-sprayed TiO_2 nanoparticles from atomized droplets were successfully deposited on the target ITO/PET surface by achieving a consolidated thin-film TiO_2 coating. Even though such particle agglomeration locally occurred on the coating, no significant porosity, crack, and delamination was observed on the resulting coating. Moreover, the EDX analysis in Fig. 11(*c*) revealed the presence of TiO_2 particles deposited on the polymer substrate. Collectively, the results confirmed the applicability of the optimized nozzle and developed spray system for the supersonic CS of nanoparticles from the atomized droplets.

Lastly, the numerical simulations and coating experiment results were compared in terms of coating width. Here, the coating width was predicted from numerical simulations by considering the trajectories of the impinging droplets onto the substrate surface in the radial direction. The width of the impinging droplet stream was calculated for the half-portion of the nozzle (see Fig. 9(*a*)), and then the obtained value was doubled (i.e., multiplied by two) due to axis symmetry to predict the actual spray width. In the experiments in Fig. 9(*b*), the coating widths were measured from five distinct locations of the coating. The calculated values were then averaged to compare the experimental results with the numerical simulations.

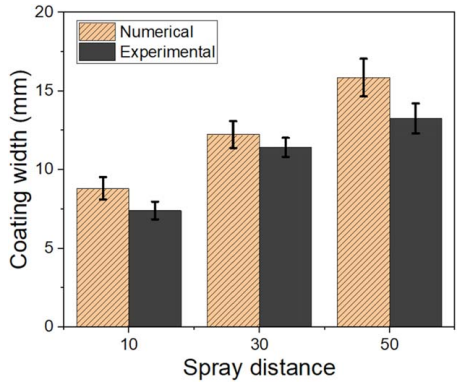

Fig. 12 Comparison of the numerical and experimental results for coating widths

Figure 12 compares the numerical simulation results with the coating experiments in terms of coating width. Both results follow a similar trend and show comparable results for spray width. The deviation in coating width increases as the SD increases. It is attributed to the falling gas velocity at higher spray distances due to the negative drag force, resulting in more particle dispersion onto the target surface [46]. The results reveal that numerical modeling in this study can be successfully used to predict the dispersion and deposition characteristics of micron-scale droplets in supersonic spray flow. Moreover, the experimental results suggest that the optimally designed supersonic nozzle and the spray system described in the present study could be successfully used to deposit the nanomaterials by utilizing droplets as the transport agent. In particular, the spray system has the potential for supersonic deposition of liquid-based functional nanomaterials (e.g., colloids and suspensions), which are challenging to deposit these important materials onto surfaces due to their low inertia.

5 Conclusion

In this study, the influence of the nozzle geometrical parameters on supersonically spraying of micron-scale droplets was investigated by numerical modeling. A discrete phase (i.e., Eulerian–Lagrangian approach) turbulent flow modeling was used to characterize the nozzle geometrical parameters for the supersonic spraying of droplets. Based on the numerical modeling results, the optimal design of the supersonic nozzle was determined and prototyped. An atomization-assisted spray system was constructed for model validation and spray coating experiments. CFD simulation results were validated through PIV measurements. The conclusions are given as follows:

- The CFD simulations revealed that the nozzle expansion ratio (d_{ex}^2/d_{th}^2) is the main factor affecting droplets acceleration under supersonic flow, followed by the divergent length.
- Micron-scale low-inertia droplets are very susceptible to turbulent velocity fluctuation of the continuous gas flow and shock waves.
- There exists an optimum nozzle expansion ratio for a set of nozzle parameters with the main influence of throat diameter and inlet gas pressure to effectively spray the droplets by mitigating the shock wave formation at the nozzle exit. This statement is true for any droplet size.
- As a noteworthy result, the optimum nozzle expansion ratio for supersonic spraying of low-inertia micron-scale "liquid droplets" differs from the expansion ratio recommended in the literature for CS of conventional "solid-state metal particles."
- To correctly accelerate the liquid droplets, the optimum nozzle expansion ratio for an axisymmetric supersonic nozzle was found to be in the range of 1.5–2.5.
- The ideal design of a supersonic nozzle for the deposition of low-inertia particles (e.g., micron-scale droplets) should possess minimum shock wave formation and optimal expansion ratio at a specific inlet gas pressure.
- The coating experiments confirmed the optimized nozzle design for supersonic spraying of droplets containing functional nanoparticles, thereby promising great potential for advanced thin-film applications.
- Despite its advantages, one possible drawback of the constructed spray system could be its limitation for the deposition of high-viscous nanoparticle solutions due to their atomization difficulty.

As for future work, the authors will test the developed supersonic spray system for various operating parameters and nanomaterial solutions (i.e., having different densities, viscosities, sizes, and shapes) and their deposition efficiency to establish a CS deposition window for nanocoating applications by minimizing trial and error processes. That would help the scalable and high-throughput

deployment of the supersonic spraying in nanocoating and advanced thin-film applications.

Acknowledgment

The first author of this study, Semih Akin, gratefully acknowledges the scholarship support by the Republic of Turkey Ministry of National Education. The authors sincerely thank Dr. Min Soo Park (SeoulTech) for his help with nozzle manufacturing. We also thank Dr. Jung-Ting Tsai (National Taiwan University) for helpful comments.

Conflict of Interest

There are no conflicts of interest.

Data Availability Statement

The datasets generated and supporting the findings of this article are obtainable from the corresponding author upon reasonable request.

Nomenclature

e = specific internal energy
g = gravitational constant
k = thermal conductivity
m = mass
n = surface normal vector
r = radius
$\mathbf{u}$ = fluid velocity
A = area
I = light intensity
P = fluid pressure
T = temperature
Y = local mass fraction of the species
$\mathbf{F}$ = force vector
$\mathbf{J}$ = mass diffusion flux in turbulent flow
d_{th} = nozzle throat diameter
d_{ex} = nozzle exit diameter
h_c = heat transfer coefficient
h_{fg} = latent heat
k_c = mass transfer coefficient
C_c = Cunningham slip correction factor
C_s = vapor concentration at the droplet surface
C_∞ = vapor concentration of the bulk flow
D_m = diffusion coefficient for species
L_{con} = nozzle convergent length
L_{div} = nozzle divergent length
S_f = source term of droplet forces
S_H = source term of evaporation energy
S_m = source term of evaporating droplet
S_y = source term of species
$\mathbf{F}_{\mathrm{Ba}}$ = Basset force
$\mathbf{F}_{\mathrm{Bu}}$ = buoyancy force
$\mathbf{F}_{\mathrm{D}}$ = Stokes drag force
$\mathbf{F}_{\mathrm{Mag}}$ = Magnus lift force
$\mathbf{F}_{\mathrm{Pg}}$ = pressure gradient force
$\mathbf{F}_{\mathrm{Saff}}$ = Saffman lift force
$\mathbf{F}_{\mathrm{VM}}$ = virtual mass force
Nu = Nusselt number
Pr = Prandtl number
Re = Reynolds number
Sc = Schmidt number

Greek Symbols

ρ = fluid density
ρ_p = particle density
μ_t = turbulent viscosity
λ = molecular mean free path
$\bar{\bar{\tau}}$ = viscous stress tensor

Abbreviations

AJP = aerosol jet printing
CFD = computational fluid dynamics
CS = cold spray
CNC = computer numerical control
DRW = discrete random walk
EDX = energy dispersive X-ray spectroscopy
ITO/PET = indium tin oxide coated polyethylene terephthalate
PIV = particle image velocimetry
SD = spray distance
SEM = scanning electron microscopy
TiO_2 = titanium dioxide

References

[1] An, S., Joshi, B., Yarin, A. L., Swihart, M. T., and Yoon, S. S., 2020, "Supersonic Cold Spraying for Energy and Environmental Applications: One-Step Scalable Coating Technology for Advanced Micro- and Nanotextured Materials," Adv. Mater., **32**(2), p. 1905028.
[2] Yin, S., Cavaliere, P., Aldwell, B., Jenkins, R., Liao, H., Li, W., and Lupoi, R., 2018, "Cold Spray Additive Manufacturing and Repair: Fundamentals and Applications," Addit. Manuf., **21**(April), pp. 628–650.
[3] Li, W. Y., and Li, C. J., 2005, "Optimal Design of a Novel Cold Spray Gun Nozzle at a Limited Space," J. Therm. Spray Technol., **14**(3), pp. 391–396.
[4] Li, W. Y., Liao, H., Douchy, G., and Coddet, C., 2007, "Optimal Design of a Cold Spray Nozzle by Numerical Analysis of Particle Velocity and Experimental Validation With 316L Stainless Steel Powder," Mater. Des., **28**(7), pp. 2129–2137.
[5] Li, W. Y., Liao, H., Wang, H. T., Li, C. J., Zhang, G., and Coddet, C., 2006, "Optimal Design of a Convergent-Barrel Cold Spray Nozzle by Numerical Method," Appl. Surf. Sci., **253**(2), pp. 708–713.
[6] Yin, S., Wang, X. F., and Li, W. Y., 2011, "Computational Analysis of the Effect of Nozzle Cross-Section Shape on Gas Flow and Particle Acceleration in Cold Spraying," Surf. Coat. Technol., **205**(8–9), pp. 2970–2977.
[7] Varadaraajan, V., and Mohanty, P., 2017, "Design and Optimization of Rectangular Cold Spray Nozzle: Radial Injection Angle, Expansion Ratio and Traverse Speed," Surf. Coat. Technol., **316**, pp. 246–254.
[8] Grujicic, M., Tong, C., DeRosset, W. S., and Helfritch, D., 2003, "Flow Analysis and Nozzle-Shape Optimization for the Cold-Gas Dynamic-Spray Process," Proc. Inst. Mech. Eng. Part B: J. Eng. Manuf., **217**(11), pp. 1603–1613.
[9] Lee, M. W., Park, J. J., Kim, D. Y., Yoon, S. S., Kim, H. Y., Kim, D. H., James, S. C., et al., 2011, "Optimization of Supersonic Nozzle Flow for Titanium Dioxide Thin-Film Coating by Aerosol Deposition," J. Aerosol Sci., **42**(11), pp. 771–780.
[10] Sova, A., Klinkov, S., Kosarev, V., Ryashin, N., and Smurov, I., 2013, "Preliminary Study on Deposition of Aluminium and Copper Powders by Cold Spray Micronozzle Using Helium," Surf. Coat. Technol., **220**, pp. 98–101.
[11] Sova, A., Smurov, I., Doubenskaia, M., and Petrovskiy, P., 2018, "Deposition of Aluminum Powder by Cold Spray Micronozzle," Int. J. Adv. Manuf. Technol., **95**(9–12), pp. 3745–3752.
[12] Jen, T. C., Li, L., Cui, W., Chen, Q., and Zhang, X., 2005, "Numerical Investigations on Cold Gas Dynamic Spray Process With Nano- and Microsize Particles," Int. J. Heat Mass Transfer, **48**(21–22), pp. 4384–4396.
[13] Champagne, V., and Helfritch, D., 2016, "The Unique Abilities of Cold Spray Deposition," Int. Mater. Rev., **61**(7), pp. 437–455.
[14] Akin, S., Wu, P., Tsai, J.-T., Nath, C., Chen, J., and Jun, M. B.-G., 2021, "A Study on Droplets Dispersion and Deposition Characteristics Under Supersonic Spray Flow for Nanomaterial Coating Applications," Surf. Coat. Technol., **426**, p. 127788.
[15] Choi, H., Lee, J. G., Mai, X. D., Beard, M. C., Yoon, S. S., and Jeong, S., 2017, "Supersonically Spray-Coated Colloidal Quantum Dot Ink Solar Cells," Sci. Rep., **7**(1), pp. 1–8.
[16] Seok Jo, H., An, S., Park, C.-W., Woo, D.-Y., Yarin, A. L., and Yoon, S., 2019, "Wearable, Stretchable, Transparent All-in-One Soft Sensor Formed From Supersonically Sprayed Silver Nanowires," ACS Appl. Mater. Interfaces, **11**(43), pp. 40232–40242.
[17] Harihara Sudhan, K., Krishna Prasad, G., Kothurkar, N. K., and Srikrishnan, A. R., 2020, "Studies on Supersonic Cold Spray Deposition of Microparticles Using a Bell-Type Nozzle," Surf. Coat. Technol., **383**(Oct.), p. 125244.
[18] Grigoriev, S., Okunkova, A., Sova, A., Bertrand, P., and Smurov, I., 2015, "Cold Spraying: From Process Fundamentals Towards Advanced Applications," Surf. Coat. Technol., **268**, pp. 77–84.
[19] Wu, H., Liu, S., Zhang, Y., and Liao, H., 2021, "New Process Implementation to Enhance Cold Spray-Based Additive Manufacturing," J. Therm. Spray Technol., **30**(5), pp. 1284–1293.

[20] ANSYS Fluent 12.1 User Guide, 2011.
[21] Sigma-Aldrich, 2021, "Silver, Dispersion Nanoparticles, 10 Nm Particle Size (TEM), 0.02 Mg/ML in Aqueous Buffer, Contains Sodium Citrate as Stabilizer," Available: https://www.sigmaaldrich.com/US/en/product/aldrich/730785.
[22] "Iron Oxide (II, III), Magnetic Nanoparticles Avg. Part. Size 10 nm, 5 mg/ML H_2O 1317-61-9," Available: https://www.sigmaaldrich.com/US/en/product/aldrich/725358.
[23] Mezhericher, M., Levy, A., and Borde, I., 2008, "Droplet-Droplet Interactions in Spray Drying by Using 2D Computational Fluid Dynamic," Drying Technol., **26**(3), pp. 265–282.
[24] Chen, C., and Zhao, B., 2010, "Some Questions on Dispersion of Human Exhaled Droplets in Ventilation Room: Answers From Numerical Investigation," Indoor Air, **20**(2), pp. 95–111.
[25] Schmidt, T., Assadi, H., Gärtner, F., Richter, H., Stoltenhoff, T., Kreye, H., and Klassen, T., 2009, "From Particle Acceleration to Impact and Bonding in Cold Spraying," J. Therm. Spray Technol., **18**(5–6), pp. 794–808.
[26] Schmidt, T., Gärtner, F., Assadi, H., and Kreye, H., 2006, "Development of a Generalized Parameter Window for Cold Spray Deposition," Acta Mater., **54**(3), pp. 729–742.
[27] Assadi, H., Kreye, H., Gärtner, F., and Klassen, T., 2016, "Cold Spraying—A Materials Perspective," Acta Mater., **116**, pp. 382–407.
[28] Hassani-Gangaraj, M., Veysset, D., Nelson, K. A., and Schuh, C. A., 2018, "In-Situ Observations of Single Micro-Particle Impact Bonding," Scr. Mater., **145**, pp. 9–13.
[29] Yin, S., Meyer, M., Li, W., Liao, H., and Lupoi, R., 2016, "Gas Flow, Particle Acceleration, and Heat Transfer in Cold Spray: A Review," J. Therm. Spray Technol., **25**(5), pp. 874–896.
[30] Alkhimov, A. P., Kosarev, V. F., and Klinkov, S. V., 2001, "The Features of Cold Spray Nozzle Design," J. Therm. Spray Technol., **10**(2), pp. 375–381.
[31] An, S., Bang, B.-H., Lee, M. W., and Yoon, S. S., 2021, "Review of Recent Progress in the Supersonic Cold-Spraying Technique With Solid Particles and Liquid Suspensions," Exp. Fluids, **62**(7), pp. 1–25.
[32] Akin, S., Lee, S., Jo, S., Ruzgar, D. G., Subramaniam, K., Tsai, J.-T., and Jun, M. B.-G., 2022, "Cold Spray-Based Rapid and Scalable Production of Printed Flexible Electronics," Addit. Manuf., **60**, p. 103244.
[33] Huang, Q., and Zhu, Y., 2019, "Printing Conductive Nanomaterials for Flexible and Stretchable Electronics: A Review of Materials, Processes, and Applications," Adv. Mater. Technol., **4**(5), pp. 1–41.
[34] Tsai, J.-T., Akin, S., Zhou, F., Bahr, D. F., and Jun, M. B.-G., 2021, "Establishing a Cold Spray Particle Deposition Window on Polymer Substrate," J. Therm. Spray Technol., **30**, pp. 1–12.
[35] Özdemir, O. Ç., Conahan, J. M., and Müftü, S., 2020, "Particle Velocimetry, CFD, and the Role of Particle Sphericity in Cold Spray," Coatings, **10**(12), pp. 1–26.
[36] Papyrin, A., Kosarev, V., Klinkov, S., Alkhimov, A., and Fomin, V. M., 2007, *Cold Spray Technology*, Elsevier Ltd., The Netherlands.
[37] Secor, E. B., 2018, "Principles of Aerosol Jet Printing," Flexible Printed Electron., **3**(3), p. 035002.
[38] Jo, S., Akin, S., Park, M. S., and Jun, M. B. G., 2022, "Selective Metallization on Glass Surface by Laser Direct Writing Combined With Supersonic Particle Deposition," Manuf. Lett., **31**, pp. 64–68.
[39] Raffel, M., Willert, C. E., Wereley, S. T., and Kompenhans, J., 2007, *Particle Image Velocimetry*, Cambridge University Press, Cambridge, UK.
[40] "VixOne™ Nebulizers | Westmed, Inc.," Available: https://westmedinc.com/vixone/.
[41] Ochowiak, M., Kasperkowiak, A., Doligalski, M., Sosnowski, T. R., Matuszak, M., Włodarczak, S., Markowska, M., Krupińska, A., and Jabłczyńska, K., 2019, "The Thermostated Medical Jet Nebulizer: Aerosol Characteristics," Int. J. Pharm., **567**, p. 118475.
[42] Misik, O., Peštálová, A., Belka, M., and Lízal, F., 2022, "Nebulizer Particle Size Distribution Measured by Various Methods," EPJ Web Conf., **264**, p. 01023.
[43] Mofakham, A. A., and Ahmadi, G., 2020, "Improved Discrete Random Walk Stochastic Model for Simulating Particle Dispersion and Deposition in Inhomogeneous Turbulent Flows," ASME J. Fluids Eng., **142**(10), p. 101401.
[44] Jaskulski, M., Wawrzyniak, P., and Zbiciński, I., 2018, "CFD Simulations of Droplet and Particle Agglomeration in an Industrial Counter-Current Spray Dryer," Adv. Powder Technol., **29**(7), pp. 1724–1733.
[45] Francia, V., Martín, L., Bayly, A. E., and Simmons, M. J. H., 2017, "Agglomeration During Spray Drying: Airborne Clusters or Breakage at the Walls?," Chem. Eng. Sci., **162**, pp. 284–299.
[46] Pattison, J., Celotto, S., Khan, A., and O'Neill, W., 2008, "Standoff Distance and Bow Shock Phenomena in the Cold Spray Process," Surf. Coat. Technol., **202**(8), pp. 1443–1454.